Nanoscale Horizons

Rich topologies of monolayer ices via unconventional electrowetting

Journal:	*Nanoscale Horizons*
Manuscript ID	NH-COM-09-2019-000619.R1
Article Type:	Communication
Date Submitted by the Author:	26-Oct-2019
Complete List of Authors:	Liu, Yuan; Beijing University of Chemical Technology Gao, Yurui; University of Nebraska-Lincoln, Department of Chemistry Zeng, Xiao Cheng; University of Nebraska-Lincoln, Department of Chemistry

New Concepts

Notion of non-conventional electrowetting is proposed for the first time. By changing the electric field of dipoles or quadrupoles embedded in the model substrates, wettability of the substrates can be tuned from superhydrophobic to superhydrophilic. At a threshold value of the dipoles or quadrupoles, water droplets can completely spread over the model substrate at ambient temperature, giving the first simulation evidence on breaking the contact-angle saturation limitation via non-conventional electrowetting. Rich topologies of monolayer ice can be obtained by changing the overall patterns of dipoles or quadrupoles on the substrate. Two new topologies of monolayer ices, namely, $4\bullet6^2$ and $4\bullet6\bullet12$, are obtained: one is stable below ambient temperature while the other is stable at the ambient temperature.

Rich topologies of monolayer ices via unconventional electrowetting

Yuan Liu[1,2], Yurui Gao[2], and Xiao Cheng Zeng[2*]

[1]*Beijing Advanced Innovation Center for Soft Matter Science and Engineering, Beijing University of Chemical Technology, Beijing 100029, China.*

[2]*Department of Chemistry, University of Nebraska-Lincoln, NE 68588, USA*

*Email: xzeng1@unl.edu

Abstract

Accurate manipulation of a substance on nanoscale and ultimately down to the level of single atom or molecule is continuously being a subject of frontier research. Herein, we show that topologies of water monolayer on the substrates, in the complete wetting condition, can be manipulated into rich forms of ordered structures via the electrowetting. Notably, two new topologies of monolayer ices are identified from our molecular dynamics simulations: one is stable below the ambient temperature while the other one can be stable at the ambient temperature. Moreover, the wettability of a substrate can be tuned from superhydrophobic to superhydrophilic by uniformly changing the charge of each atomic site of the dipole or quadrupole distributed orderly on the model substrate. At a certain threshold value of the atomic charge, water droplets on the substrate can spread out spontaneously, achieving the complete electrowetting. Importantly, unlike the conventional electrowetting which invokes uniform external electric field, we propose non-conventional electrowetting, for the first time, via invoking the electric field of dipoles and quadrupoles embedded in the substrate. While different topologies of water monolayer can be achieved by the non-conventional electrowetting. A major advantage of the non-conventional electrowetting is that the contact-angle saturation, a long-standing and known limitation in the field of electrowetting, can be overcome by tuning uniformly the lattice atomic charge at the surface, thereby offering a new way to mitigate the contact-angle saturation for various electrowetting application.

INTRODUCTION

Miniaturization is a trend in today's science and technology. Integration and automation of many processes on a single device with micro- or even nano-scale size have already been implemented in various electronic devices or lab-on-a-chip systems.[1] Manipulation of a substance on nanoscale and ultimately down to the level of single atom or molecule is continuously being a subject of intense research. Water is ubiquitous and can be found on nearly all surfaces in natural systems or in technology devices. On artificial surfaces, water droplets have been successfully manipulated through controlling the wettability and surface structures, *e.g.* moving along a certain path on surfaces, splitting, merging and mixing with a high degree of flexibility, translating and vertical bouncing or jumping on a surface.[1-9] Here, a non-conventional electrowetting is proposed by applying the electric field onto a water droplet via the embedded dipoles and quadrupoles in the substrate, rather than using the uniform external electric field as in the conventional electrowetting. First, we show that a long-standing limitation of the contact-angle saturation in electrowetting[10] can be overcome by the non-conventional electrowetting. Second, we show that the topologies of water monolayer on the substrates can be manipulated into rich forms of ordered structures via the non-conventional electrowetting, as the latter can tune the wettability of the substrate by altering the magnitude of surface dipoles or quadrupoles.

The contact-angle saturation refers to the phenomenon that the contact angle of water droplets converges to a non-zero value as the voltage increases during the conventional electrowetting. This behavior limits the performance of the conventional electrowetting-on-dielectrics (EWOD) devices because the maximal tunable range of the contact angle in EWOD dictates performance of the devices based on the conventional electrowetting technology.[10-13] It is important to overcome the limitation of the contact-angle saturation so that the functionality of many devices can be enhanced, thereby leading to, e.g., larger numerical aperture of the liquid lens, higher efficiency of the digital microfluidics, or higher brightness of electronic displays. [10-13] Various explanations to the contact-angle saturation have been proposed,[10-12] but lacking of studies to resolve this issue until now. Recently Li *et al.*[11] presented a method

to lower the contact-angle saturation value by controlling the charge trapping at the liquid-solid interface. He *et al.*[14] reported low-voltage electrowetting on slippery lubricant-infused porous surface and attempted to attain a large modulating range of the contact angle. In addition, electrowetting at nanoscale was studied using molecular dynamics (MD) simulations.[6, 7, 15-17] It was shown that contact angles of water nano-drops on graphite surface are sensitive to the polarity (positive or negative) and direction (parallel or perpendicular) of the applied electric field.[15] Ren *et al.*,[17] indicated that the interfacial structures and wetting properties of water droplets on graphene surface were highly sensitive to the external electric field. Wetting properties of water droplets on a hydrophilic silica substrate subjected to various electric fields were also investigated.[16] Giovambattista *et al.*[18] demonstrated that the hydrophobicity and hydrophilicity of the solid model surface based on silica can be tuned by the surface polarity from MD simulations. Yuan and Zhao studied the dynamics of electrowetting on pillar-arrayed surfaces and a smooth surface by using MD simulations.[19, 20]

Understanding surface and interfacial water and ice has important implications to many fundamental areas, *e.g.* heterogeneous catalysis, electrochemistry, corrosion, and lubrication, *etc*.[21, 22] Extensive studies of structures of interfacial water/ice have been reported in the literature.[23-30] On metal surfaces, monolayer (ML) ice can be deposited at cryogenic condition (*e.g.* ~130 K).[26-28] A buckled hexagonal monolayer ice was observed on Pt (111) surface, [24, 26] while Ogasawara *et al.*[31] showed that the 2D ordered hexagonal water layer on Pt (111) was flat without uncoordinated OH groups. Kimmel *et al.*[27] also demonstrated the water monolayer on Pt (111) exhibits no dangling OH bonds or lone pair electrons. Pentagons and heptagons could also arise in the hexagonal water network on Pt (111), as demonstrated by Nie *et al.*[28], without 3D island growing on top of the first wetting layer.[28] Hexagonal water networks were also found on the surface of Cu (111).[32] On the surface of Ru (001), partially dissociated water overlayer was identified.[33, 34] An ordered water monolayer with mixed H_2O/OH was also detected on the surface of MgO (001).[35] On the hydrophilic mineral surfaces, monolayer ice structures were also observed, *e.g.* an ice-like ordered H-bonded network without dangling OD groups was revealed on the surface of mica by Miranda *et al.*[36] A well-

ordered monolayer ice with tetragonal and octagonal patterns of H-bond network on hydroxylated silica surface was predicted by Yang *et al*.[37] On NaCl (001) surface, an unconventional monolayer ice with a regular array of Bjerrum *D*-type defects was found below 145 K.[38] On graphite surface, a hexagonal monolayer ice without shared edges was recently observed at 150-160 K.[39] In addition, various monolayer ice phases were predicted to exist between two hydrophobic surfaces below room temperature, such as planar hexagonal, Archimedean $4•8^2$, planar rhombic, puckered rhombic, and irregular pentagonal.[40-44] Like rich crystalline phases of 3D bulk ices,[45, 46] water can form a variety of topological structures of 2D ices either on solid surfaces or in nanoscale confinement.[40, 47]

More specifically, in this study, we show that at ambient temperature water droplets can completely spread out on a solid model substrate with the non-conventional electrowetting. We provide the first simulation evidence that the contact-angle saturation limitation can be fully eliminated in non-conventional electrowetting. We also show that different topologies of monolayer ice can be obtained by manipulating the patterns of dipoles and quadrupoles on the substrate. For example, two previously known monolayer (ML) ices, 6^3 and $4•8^2$, can be spontaneously formed from water droplets on solid model substrates at room temperature, contrasting to the water molecules deposition on metal or on graphene surface at cryogenic condition, or to the spontaneous formation of ML ice in nanoscale confinement condition. More importantly, two new topologies of ML ices are observed in our MD simulations: one is stable below the room temperature while the other one can be stable at room temperature. The two new structures are named as $4•6^2$ and 4•6•12 ML ice according to the specific tiling from regular polygons.

RESULTS AND DISCUSSION

Overcoming the contact-angle saturation in electrowetting

The method of electrowetting is to change the contact angle of an electrolyte via an applied electric field with respect to the interface between the solid and the electrolyte.[1, 3, 10] Instead of using a uniform external electric field in the conventional electrowetting,

here, a non-conventional electrowetting is proposed by applying an orderly patterned electric field onto a water droplet via the underlying dipoles and quadrupoles embedded in the substrate. As such, arrangement of water molecules in the complete wetting state can be manipulated through different patterns of dipoles or quadrupoles. As depicted in Electronic Supplementary Information (ESI) Fig. S1A, the atomic structures of the substrate models resemble Au (111) and Au (100). The results presented in this work can be generic for a class of surfaces with similar atomic arrangements. As depicted in Fig. 1, the wettability of the substrate can be tuned from being superhydrophobic to superhydrophilic simply by increasing magnitude of all atomic charges q. The original model substrate is superhydrophobic without any embedded dipoles, evidenced by the largest contact angle of 170° for a water nanodroplet. The substrate becomes hydrophilic with a contact angle of 37° for the water nanodroplet at 300 K, after increasing the magnitude of atomic charge on each site of the dipole to q = 0.4. Interestingly, a monolayer ice arises spontaneously on the substrate when the magnitude of the atomic charge q is increased to 0.5 while the temperature is controlled at 300 K, and eventually the substrate could be completely covered by the 2D ice in hundreds of nanoseconds. To speed up this process, several smaller droplets can be used instead of a single droplet (see Movie S1). At the temperature of 270 K, 330 K, and 350 K, the atomic charge q for the spontaneous formation of monolayer ice is 0.6, 0.5, and 0.5, respectively (see Fig. S2).

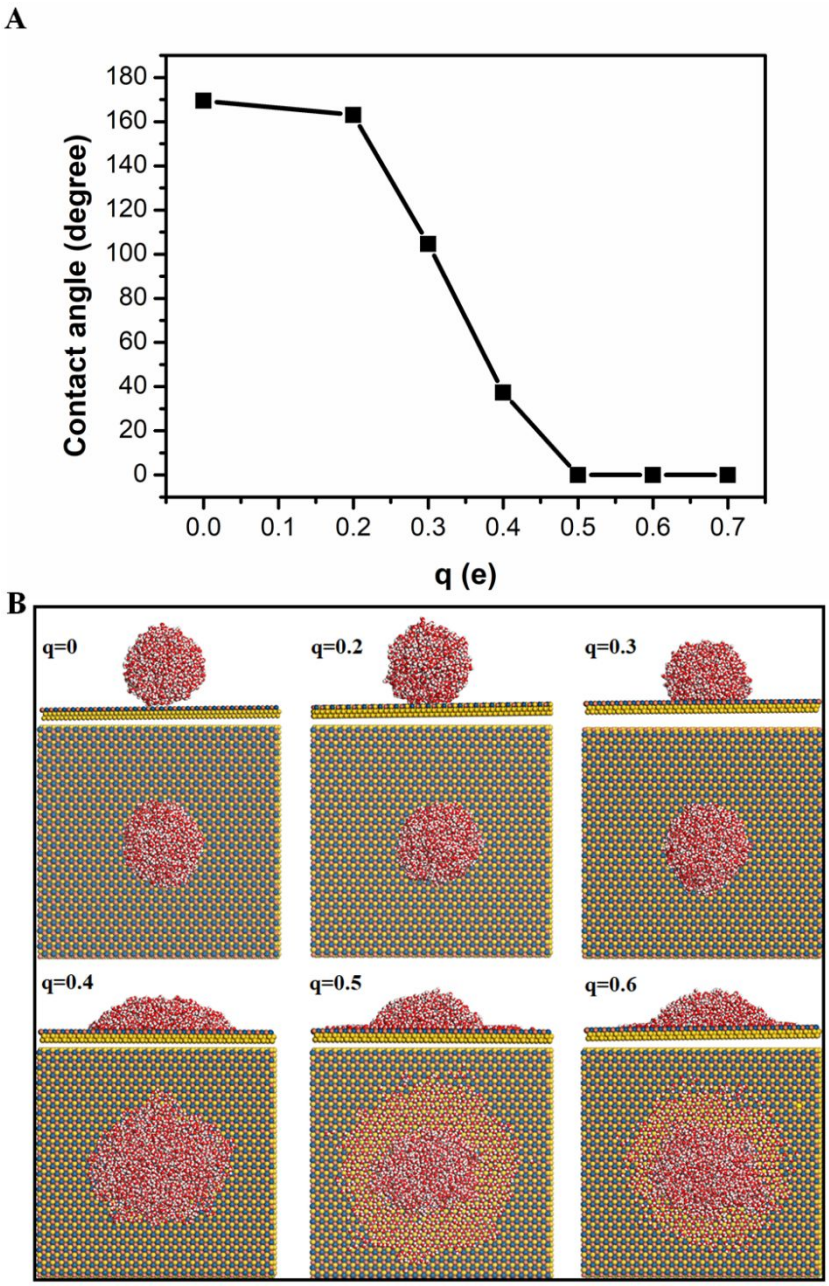

Fig. 1 (**A**) Contact angle of a water nanodroplet (at 300 K) on a model substrate *versus* the atomic charge associated with each site of a dipole by using the non-conventional electrowetting with the electric field produced from the uniformly dispersed dipoles on the substrate. (**B**) Side view (upper panel) and top view (lower panel) of a snapshot for each case of atomic charge. The atomic structure of the substrate resembles that of Au (111) surface, where pink and light blue atoms have a charge of +q and -q, respectively; yellow atoms are neutral atoms, red and white atoms are oxygen and hydrogen atoms of water molecules, respectively.

In addition to the substrate shown in Fig. S1A, water droplets on three other substrates presented in Fig. S1B-S1D can also completely wet these substrates at room temperature. In other words, the contact angle of water droplets become zero on these

four model substrates. Hence, we demonstrate, for the first time, that the limitation of the contact-angle saturation in conventional electrowetting can be overcome by the non-conventional design using a substrate with uniformly dispersed dipoles or quadrupoles. Based on the previous experimental studies, the contact-angle saturation in electrowetting is due to the trapped charges at the liquid-solid interface once the external electric field is applied.[11] An electric field is induced by the trapped charges at the liquid-solid interface, whose direction is opposite to the external electric field. Thus, the contact-angle saturation phenomenon is inevitable in the conventional electrowetting. In this work, only one electric field is presence, produced by the patterned dipoles/quadrupoles on the substrates. As such, the contact-angle saturation phenomenon is avoided by the unconventional design. This conceptual advancement opens the possibility to resolve the contact-angle saturation restriction in practical electrowetting systems by design.

Four topologies of monolayer ices on the model substrates

Fig. 2A depicts structure of the 6^3 ML ice, a flat monolayer similar to the previously observed hexagonal ML ice on Pt (111) through vapor deposition (but slightly different from the ML ice structure obtained in nanoscale confinement under uniform and in-plane electric field).[40, 41] Each water molecule in the 6^3 ML ice has three H_2O nearest neighbors, while the dangling H-bonds point to the substrate. The distance between the center of oxygen atom of H_2O and the center of atoms in first atomic layer of the substrate is 2.35 Å (Table 1). While the hexagonal ML ice observed on the surface of Pt (111) at cryogenic temperature[27, 31] is formed from vapor deposition, the 6^3 ML ice here is spontaneously formed from water droplets at 300 K on the model substrates (Movie S1).

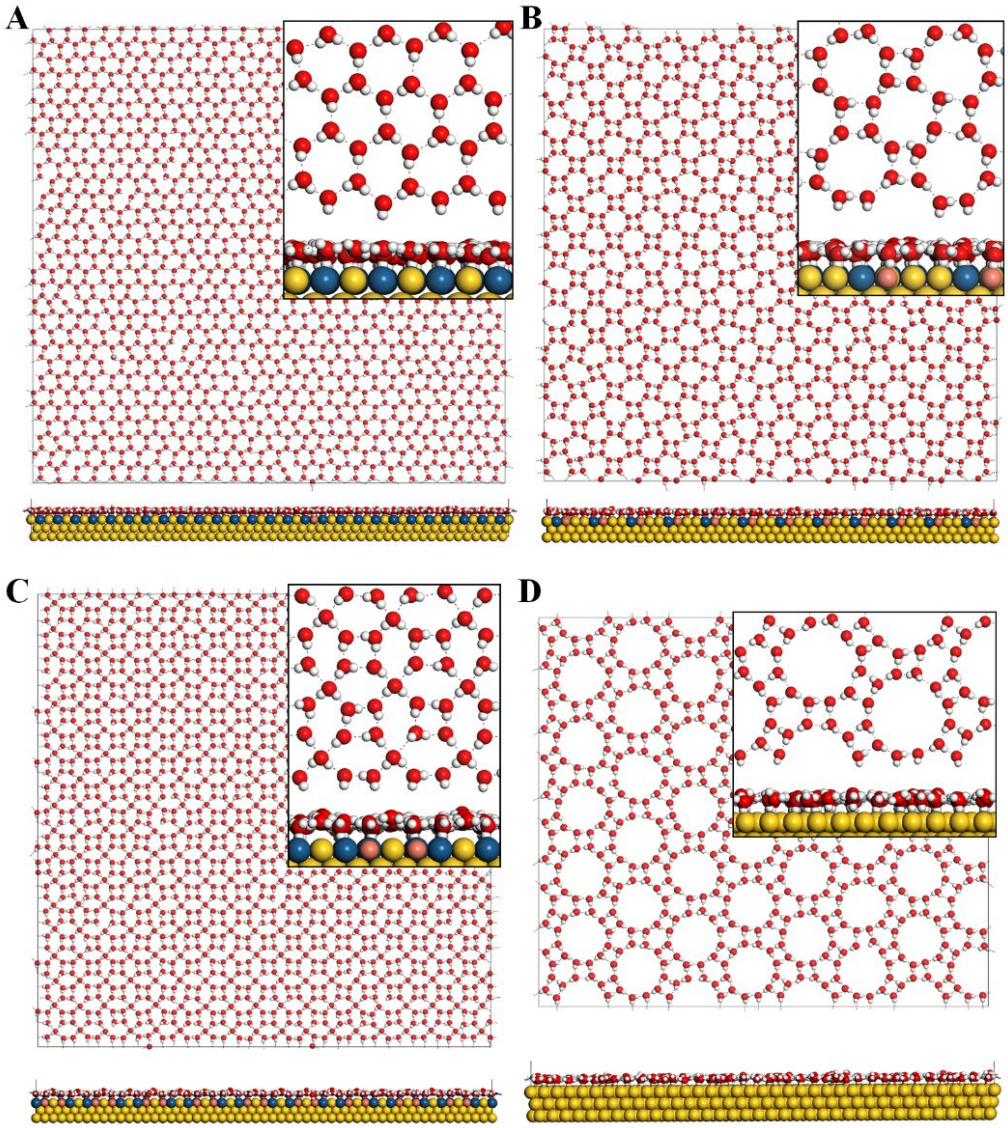

Fig. 2 Structures of monolayer (ML) ice on model substrates with dispersed dipoles or quadrupoles. (**A**) 6^3 ML ice at 300 K, (**B**) $4{\bullet}8^2$ ML ice at 300 K, (**C**) $4{\bullet}6^2$ ML ice at 200 K, (**D**) 4•6•12 ML ice at 300 K. The charge q on each site of dipole or quadrupole is ±0.6e, insets are zoomed-in images.

Fig. 2B displays the $4{\bullet}8^2$ monolayer ice with tetragons and octagons, obtained on a model substrate with dispersed quadrupoles. Again, each water molecule in the $4{\bullet}8^2$ ML ice has three H_2O nearest neighbors, while the dangling H-bonds point to the substrate, similar to ice tessellation reported on the hydroxylated silica surface.[37] The pattern of the oxygen is also the same as that of the guest-free monolayer clathrate ice with $4{\bullet}8^2$ *Archimedean* tiling obtained in nanoscale confinement below room

temperature.[42] As in the case of the 6^3 ML ice, the $4•8^2$ ML ice can also be spontaneously formed from water nanodroplets at 300 K on the model substrate with dispersed quadrupoles (Movie S2).

Two previously unreported ML ices are also obtained on model substrates with different patterns of quadrupoles. Fig. 2C and Fig. S1C display the $4•6^2$ ML ice with tetragons and hexagons shown in H-bonded water network. Here, two types of H-bonded water molecules are seen: One is four H-bonded H_2O, and the other one is three H-bonded H_2O with the dangling bonds pointing to the substrate. As shown in Table 1, the four H-bonded H_2O molecules are located ~0.6 Å further away from the substrate. Fig. 2D and Fig. S1D display the 4•6•12 ML ice with tetragons, hexagons, and dodecagons shown in H-bonded water network. This is a flat ML structure with all the dangling bonds of the three H-bonded H_2O pointing to the substrate. As in the case of 6^3 and $4•8^2$ ML ice, the 4•6•12 ML ice can also be spontaneously formed from water nanodroplets at 300 K on the model substrates with dispersed quadrupoles (Movie S3). As shown in Fig. S3 and Movie S4, the 4•6•12 ML ice can also be spontaneously obtained from a water droplet at 300 K on the graphene surface with ±0.6e charges fixed on the carbon atoms according to the quadrupole pattern in the model substrate.

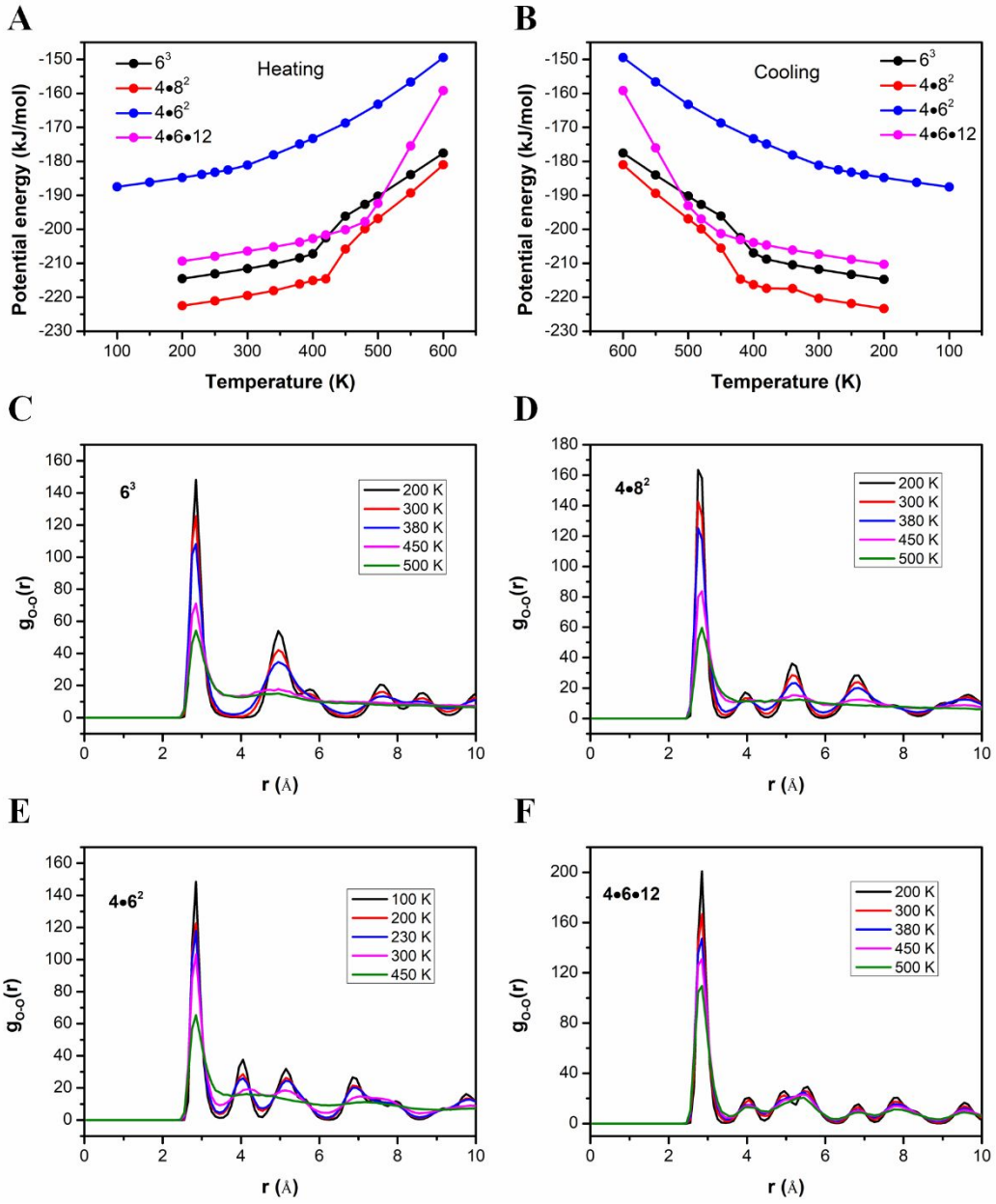

Fig. 3 Potential energies per water molecule for 6^3, $4•8^2$, $4•6^2$, and 4•6•12 ML ices *versus* the temperature in the heating (**A**) and cooling (**B**) process, respectively. Radial distribution function (RDF) of the O-O atoms of water molecules for (**C**) 6^3, (**D**) $4•8^2$, (**E**) $4•6^2$, and (**F**) 4•6•12 ML ices at various temperature in the heating process.

Fig. 3A and 3B show plots of potential energies per water molecule of each ML ice *versus* the temperature of the system in the heating and cooling processes, respectively. Since the number of atoms, dipoles or quadrupoles on the model substrates are different, the potential energy values cannot be used to assess relative stabilities

among the four ML ices. Nevertheless, for all the four ML ices, the same trend is obtained, i.e., the potential energy per molecule is higher as the temperature increases in the heating process (Fig. 3A). As shown in Fig. S4-S7, defects are observed after the temperature exceeds a certain threshold value, e.g., ~300 K for both the 6^3 and $4•8^2$ ML ices, 230 K for the $4•6^2$ ML ice, and 380 K for the 4•6•12 ML ice. In the cooling process from 600 K, water vapor deposition is observed as shown in Fig. S8-S11. Nearly defect-free structures of both the 6^3 and $4•8^2$ ML ices are obtained at 300 K (see Fig. S8 and S9). In the case of $4•6^2$ ML ice, however, many 5/7/8-rings topological defects are seen during the vapor deposition as shown in Fig. S10, suggesting the $4•6^2$ ML ice may be a metastable structure. Notably, defect-free structure of the 4•6•12 ML ice can be achieved at 380 K from the vapor deposition in the cooling process, as shown in Fig. S11. Overall, the potential energies per molecule decrease as the temperature decreases (see Fig. 3B).

Table 1 Physical parameters of ML ices obtained in this work. Here, x and y refer to the lattice parameter in the direction of x and y; N_{H2O}, N_{sub}, and N_{pole} denote the number of water molecules, the number of substrate atoms, and the number of dipoles or quadrupoles on the model substrate, respectively; d_{OO} and $d_{O\text{-}sub}$ denote the nearest O-O distance and the distance between oxygen atoms of H_2O and the first-layer substrate atoms.

ML ice	$\mathbf{6^3}$	$\mathbf{4•8^2}$	$\mathbf{4•6^2}$	**4•6•12**
x/Å	134.74	115.17	124.08	93.51
y/Å	129.66	115.17	124.08	80.98
N_{H2O}	1620	1152	1620	576
N_{sub}	7290	6912	8748	11664
N_{pole}	810	288	324	144
d_{OO}/Å	2.90	2.85	2.90	2.88
$d_{O\text{-}sub}$/Å	2.35	2.38	2.34, 2.89	2.51

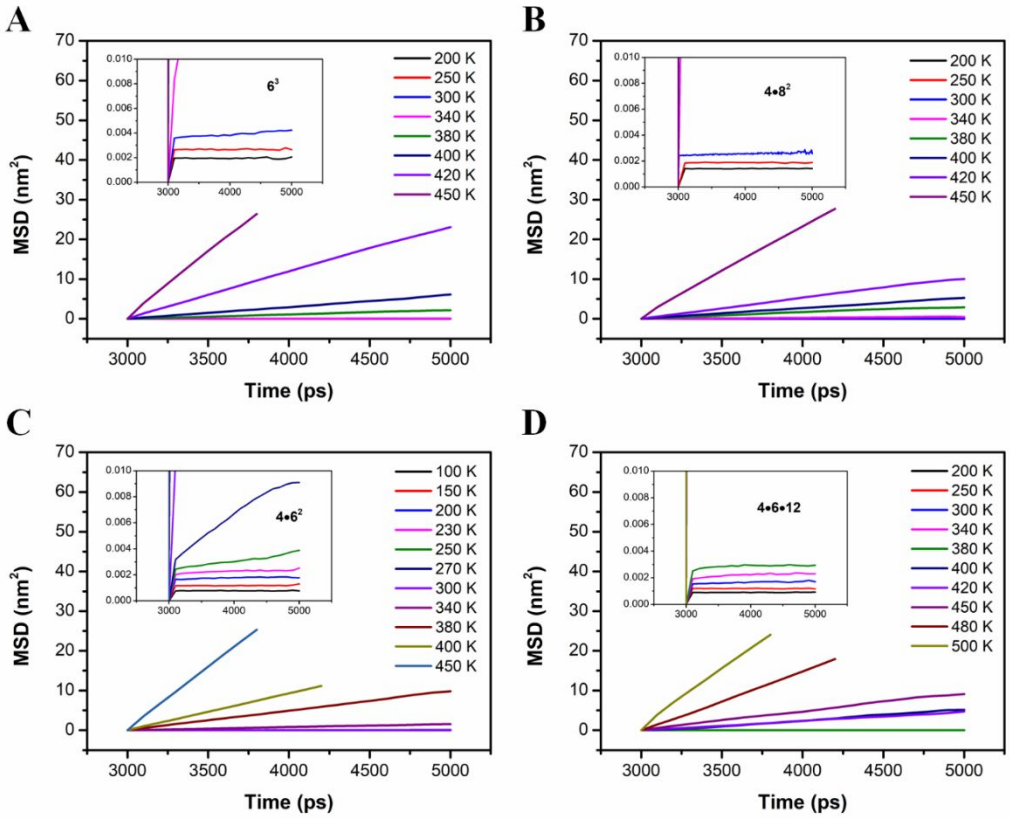

Fig. 4 Mean-square displacement (MSD) of (**A**) 6^3, (**B**) $4•8^2$, (**C**) $4•6^2$, and (**D**) 4•6•12 ML ices at various temperatures in the heating process. Insets are zoomed-in plot in the range of 0-0.01 nm^2 along the vertical axis.

To analyze the structure properties and structural stabilities of the ML ices, radial distribution functions (RDF) and mean square displacements (MSD) of each phase are computed at various temperature as shown in Figs. 3 and 4. The first peaks in RDF are located at 2.85-2.90 Å (Fig. 3C-3F), consistent with the nearest O-O distance of the ML ices listed in Table 1, as well as that of ML ices from previous reports.[40] Following a definition of the structure order parameter reported in a previous study,[48] here, the calculated order parameter *S* are -0.22, -0.22, -0.28, and -0.22 for the 6^3, $4•8^2$, $4•6^2$, and 4•6•12 ML ices, respectively. The structural stability of ML ice decreases as the temperature increases as reflected by the height of the first peaks which becomes lower as the temperature increases. Structural stabilities of each ML ices are also manifested by the MSD. Both 6^3 and $4•8^2$ ML ice are intact until 300 K, as reflected by low slope of MSD curves (Fig. 4A and 4B). Increasing number of defects arise gradually at 340

K and 380 K as shown in Figs. S4 and S5. Note that for the TIP4P/ICE water potential employed in this work, the computed ice Ih melting point is 272 K at 1 bar.[49] Thus, both 6^3 and $4•8^2$ ML ice are stable at ambient temperature. As shown in Fig. 4C, the $4•6^2$ ML ice is stable at 230 K, corresponding to the temperature of supercooled water. Increasing number of defects gradually arise from 250 K to 270 K, as shown in Fig. S6. Thus, the $4•6^2$ ML ice cannot be stable at room temperature as other ML ices. Notably, the 4•6•12 ML ice exhibits the highest structural stability, whose structure is still intact even at elevated temperature of 380 K, as shown in Figs. 4D and S7.

Formation of $4•6^2$ and 4•6•12 monolayer ices on surface of realistic materials

To examine if the ML ices could be realized in the laboratory, we considered surface of realistic materials with similar distribution of surface dipoles/quadrupoles to our model substrates. As reported by Wang *et al.*,[50] InSb (110) surface has similar dipole distribution as the model substrate for 6^3 ML ice. Thus, the 6^3 ML ice may be formed on the InSb (110) surface at low temperature. As reported by Meng *et al.*,[51] on the H-terminated diamond (111) surface, the original hydrophobic behavior can be tuned to be superhydrophilic by replacing the hydrogen atoms to Na and F atoms. Hence, the ML ices may be formed on Li- or Na- and F- or Cl-terminated diamond (100) and (111) surfaces with the pattern of the dipoles/quadrupoles akin to the model substrates considered here. Motivated by the ice tessellation (i.e., $4•8^2$ ML ice in this work) on a hydroxylated silica surface,[37] we modified the H-terminated diamond (100) by replacing some of the hydrogen atoms with OH groups and O atoms as shown in Fig. S12A. Our DFT structural optimization (based on PBE-D3 functional) suggests that the $4•6^2$ ML ice is still stable on the modified surface (Fig. 5A). In addition, at 150 K, the 20 ps *ab initio* molecular dynamics (AIMD) simulation also suggests the $4•6^2$ ML ice is stable (Movie S5).

Moreover, as shown in Fig. S3 and Movie S4, the 4•6•12 ML ice can be spontaneously formed from a water nanodroplet at 300 K on the graphene model surface with positive and negative atomic charges fixed on the carbon atoms. Aside from the artificially charged graphene surface, the 4•6•12 ML ice is also found to be

stable on the boron- and nitrogen-doped graphene surface (see Fig. S12B), as demonstrated from the PBE-D3 optimized structure (Fig. 5B). In addition, the 4•6•12 ML ice structure is intact at 200 K for 20 ps, based on the AIMD simulation (see Movie S6). In sum, the ML ices reported in this work are likely be achieved in realist surfaces, as in the case of formation of bilayer hexagonal ice observed on Au(111) surface.[52]

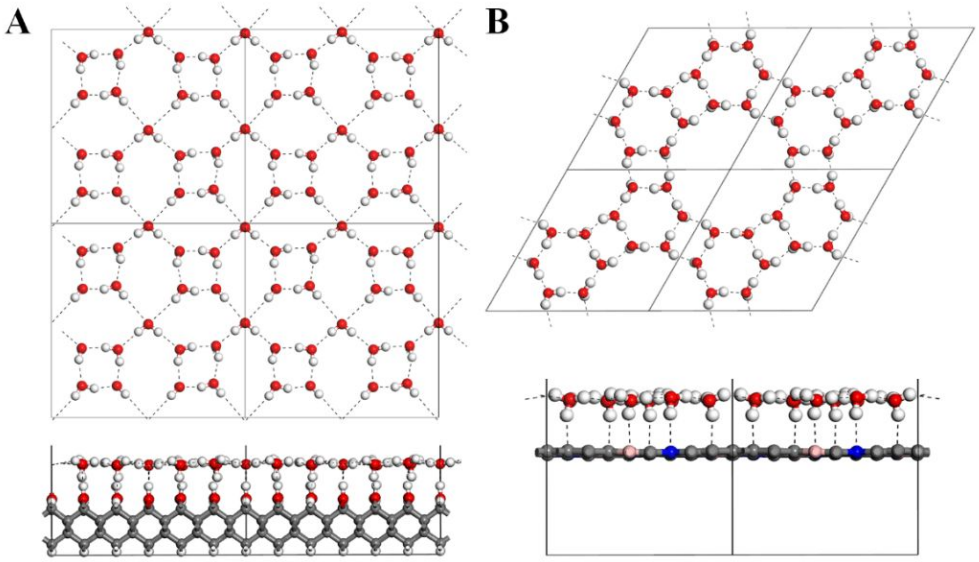

Fig. 5 Structural optimization of the 4•6^2 and 4•6•12 ML ice structures on surface of realistic materials (atoms of substrate are fixed), using dispersion corrected PBE-D3 functional. (**A**) The 4•6^2 ML ice on the H-terminated surface of diamond (100) with OH and O modification at certain atomic positions. (**B**) The 4•6•12 ML ice on the graphene surface with boron and nitrogen atoms doped at certain atomic positions. The upper panel is the top view of the structure with the substrate unseen, and the lower panel is the side view of the structure. Red and white balls represent oxygen and hydrogen atoms, respectively. Grey, blue, and light pink balls represent carbon, nitrogen, and boron atoms, respectively. Dashed black lines represent the hydrogen bonds, and the solid black line represent the lattice of the unit cell.

CONCLUSIONS

In this study, we have shown that the wettability of the solid substrate can be easily tuned from superhydrophobic to superhydrophilic by changing the dipoles or quadrupoles embedded on the model substrate. At a certain threshold value of the atomic charge, water nanodroplets on the substrate can be spontaneously spread out (in complete wetting state), at which the contact angle of the water droplet turns into zero. As such, the contact-angle saturation, a long-standing limit for electrowetting, can be overcome. Indeed, this non-conventional surface modification strategy opens an avenue to overcome the contact-angle saturation in practical electrowetting. We also show that water molecules can be manipulated into different arrangements with highly ordered ML topologies via the non-conventional electrowetting. We observe that both 6^3 and $4•8^2$ ML ices can be formed spontaneously from water nanodroplets at ambient condition on model substrates with uniformly embedded dipoles or quadrupoles. Two new topologies ($4•6^2$ and 4•6•12) of ML ices are reported on the model substrates with uniformly embedded dipoles or quadrupoles, one is stable below the room temperature and the other one can be stable at room temperature. Thus far, previously reported 2D ices are either formed from vapor deposition in cryogenic environment or formed spontaneously in nanoscale confinement. Importantly, we demonstrate that the two ML-ice structures can be formed on surfaces of more realistic materials based on DFT optimization and AIMD simulations, thereby suggesting high likelihood for future experimental confirmation of the two ML-ice structures.

METHODS

Model substrates for non-conventional electrowetting

To construct the model substrates, Au (111) and Au (100) surfaces with three atomic layers are selected as the templates. Next, dipoles or quadrupoles are uniformly embedded in the first atomic layer, as shown in Fig. S1. The wettability of the substrate can be tuned by changing the atomic charge on each site of the dipoles or quadrupoles to indirectly alter the magnitude of the electric field applied onto the droplets, contrasting to the conventional electrowetting (for which the magnitude of the electric field is directly tuned). Hence, the electric field acting onto the water droplets is produced from the dipoles and quadrupoles embedded in the substrate. The substrate is superhydrophobic if the site charge of dipoles or quadrupoles is zero.

As listed in Table 1, structure parameters of four monolayer ice topologies on different substrates with embedded dipoles/quadrupoles are presented. To achieve the 6^3 monolayer ice, the size of the substrate (supercell) is 13.47 nm × 12.97 nm, consisting of 7290 atoms and 810 dipoles (see Fig. S1A). To achieve the $4•8^2$, $4•6^2$, and 4•6•12 ML ices, the sizes of substrates are 11.52 nm × 11.52 nm, 12.41 nm × 12.41 nm, and 9.35 nm × 8.10 nm, respectively, and the corresponding system consists of 6912 atoms with 288 quadrupoles, 8748 atoms with 324 quadrupoles, and 11664 atoms with 144 quadrupoles (see Fig. S1B-D). Except the substrate in the 6^3 case with the original Au lattice, the substrates used in the $4•8^2$, $4•6^2$, and 4•6•12 cases are laterally compressed by 17%, 20%, and 48%, respectively, from the original bare Au substrate in order to make the average length of positive-negative charges around 2.8 Å. In addition, taken the 6^3 ML ice on Au (111) and the $4•8^2$ ML ice on Au (100) as two examples, the suitable range of lattice constants for the Au-like FCC substrate is studied. For the 6^3 ML ice on Au (111), the suitable lattice constants of Au-like FCC substrate range from 3.82 to 4.24 Å, with the corresponding nearest O-O distance ranging from 2.7 to 3.0 Å. For the $4•8^2$ ML ice on Au (100), the suitable lattice constants of Au-like FCC substrate range from 3.25 to 3.68 Å, with the averaged distance of the nearest O-O ranging from 2.78 to 3.14 Å.

Molecular dynamics simulations

The total number of H_2O molecules in water droplets in the four ML ice cases are 1620, 1152, 1620, and 576, respectively, and these number of water molecules can fully cover the corresponding four substrates. TIP4P/ICE water potential is employed to describe the interaction of H_2O, which has been shown to give reasonable densities and phase diagram of various crystalline ices.[49] The melting point of TIP4P/ICE ice Ih at 1 bar is 272 K,[49] very close to the experimental value of 273 K. The interaction between substrate atoms and water molecules is represented by a 12-6 Lennard-Jones (LJ) potential with parameters 3.2 Å for $\sigma_{O\text{-}sub}$ and 0.1 kJ/mol for $\varepsilon_{O\text{-}sub}$. To adjust the wettability of the model substrates, the magnitude of atomic charge q on each site of dipole is gradually increased from 0, in a step of 0.1 e. The ML ice starts to form for $q \geq 0.5$. Typically, hundreds of nanoseconds are needed such that the ML ice can completely cover the substrate. The process can be speeded up by using multiple water droplets with smaller size, instead of using a single large-droplet.

For the contact-angle computation, the method described in Ref. 50[53] is used. MD simulation with 5 ns for each case is carried out with the first 3 ns being used to reach equilibrium, while the trajectory of the last 2 ns is used for analysis. For stability studies of each ML ice, 5 ns MD simulation is carried out with q being 0.6 e at each temperature, and the last 2 ns of each trajectory is used for computing the radial distribution function (RDF) and mean-square-displacement (MSD). All MD simulations are performed in the *NVT* ensemble at various temperatures. Periodic boundary condition (PBC) is used. To neglect interactions among imaging systems, a value of 14.7 nm in z direction (vertical direction to the substrate) is employed. Fast smooth particle-mesh Ewald method is used for electrostatic interactions with a real-space cutoff of 10 Å. The van der Waals interactions are truncated at 10 Å. A leap-frog algorithm for integrating Newton's equations of motion with a time step of 1 fs is employed for the MD simulations. The constant temperature is controlled by using Nosé-Hoover scheme with a chain length of 10 and a temperature coupling constant of 0.5 ps. All the classical MD simulations are carried out by using the Gromacs 4.6.5 software.[54]

***Ab initio* molecular dynamics simulation (AIMD)**

The supercell of diamond (100) with the size of 15.18 Å ×15.18 Å ×24.47 Å and lattice

angles of α = β = γ = 90° are used as the model substrate for the 4•6^2 ML ice (see Fig. S12A and 5A). The boron and nitrogen doped graphene with a supercell size of 12.78 Å ×12.78 Å × 25 Å and lattice angles of α = β = 90° and γ=120° are used as the substrate for the 4•6•12 ML ice (see Fig. S12B and 5B). The simulation systems are firstly optimized with the substrate atoms being fixed. Dispersion-corrected PBE-D3[55] functional implemented in the QUICKSTEP program of the CP2K package is employed.[56] The GPW (Gaussian and Plane Waves)[57] method and the GTH (Goedecker-Teter-Hutter)[58, 59] norm-conserving pseudopotential are adopted in DFT computations. A combination of Gaussian DZVP[60] basis set and auxiliary plane waves with energy cutoff of 300 Ry are used to expand the electron density. For the AIMD simulations, the *NVT* ensemble with time step of 1 fs is used, and the Nosé-Hoover chain method is used to control the system temperature. Trajectories of 20 ps for the 4•6^2 ML ice at 150 K and 20 ps for the 4•6•12 ML at 200 K are obtained from the AIMD simulations.

Acknowledgements. YL was supported by the National Natural Science Foundation of China (No. 21703006), by China Postdoctoral Science Foundation (No. 2017M620582). XCZ was supported by US NSF (CHE-1665324) and Nebraska Center for Energy Sciences Research at UNL, and by University of Nebraska Holland Computing Center.

REFERENCES

1. F. Mugele and J. C. Baret, *J. Phys. Condens. Matter*, 2005, **17**, R705-R774.
2. M. Joanicot and A. Ajdari, *Science*, 2005, **309**, 887-888.
3. F. Mugele, M. Duits and D. van den Ende, *Adv. Colloid Interface Sci.*, 2010, **161**, 115-123.
4. D. R. Link, E. Grasland-Mongrain, A. Duri, F. Sarrazin, Z. D. Cheng, G. Cristobal, M. Marquez and D. A. Weitz, *Angew. Chem. Int. Ed.*, 2006, **45**, 2556-2560.
5. S. K. Cho, H. J. Moon and C. J. Kim, *J. Microelectromech. Syst.*, 2003, **12**, 70-80.
6. S. Datta, A. K. Das and P. K. Das, *RSC Adv.*, 2016, **6**, 9796-9802.
7. J. Zeng, S. W. Zhang, K. R. Tang, G. Chen, W. Yuan and Y. Tang, *Nanoscale*, 2018, **10**, 16079-16086.
8. P. R. C. Gascoyne, J. V. Vykoukal, J. A. Schwartz, T. J. Anderson, D. M. Vykoukal, K. W. Current, C. McConaghy, F. F. Becker and C. Andrews, *Lab on a Chip*, 2004, **4**, 299-309.

9. M. G. Pollack, A. D. Shenderov and R. B. Fair, *Lab on a Chip*, 2002, **2**, 96-101.
10. A. Quinn, R. Sedev and J. Ralston, *J. Phys. Chem. B*, 2005, **109**, 6268-6275.
11. X. M. Li, H. M. Tian, J. Y. Shao, Y. C. Ding, X. L. Chen, L. Wang and B. H. Lu, *Adv. Funct. Mater.*, 2016, **26**, 2994-3002.
12. D. Klarman, D. Andelman and M. Urbakh, *Langmuir*, 2011, **27**, 6031-6041.
13. Y. Y. Guo, Y. Deng, B. J. Xu, A. Henzen, R. Hayes, B. Tang and G. F. Zhou, *Langmuir*, 2018, **34**, 11943-11951.
14. X. D. He, W. B. Qiang, C. Du, Q. F. Shao, X. P. Zhang and Y. Q. Deng, *J. Mater. Chem. A*, 2017, **5**, 19159-19167.
15. C. D. Daub, D. Bratko, K. Leung and A. Luzar, *J. Phys. Chem. C*, 2007, **111**, 505-509.
16. F. H. Song, L. Ma, J. Fan, Q. C. Chen, G. P. Lei and B. Q. Li, *Phys. Chem. Chem. Phys.*, 2018, **20**, 11987-11993.
17. H. R. Ren, L. N. Zhang, X. Y. Li, Y. F. Li, W. K. Wu and H. Li, *Phys. Chem. Chem. Phys.*, 2015, **17**, 23460-23467.
18. N. Giovambattista, P. G. Debenedetti and P. J. Rossky, *J. Phys. Chem. B*, 2007, **111**, 9581-9587.
19. Q. Z. Yuan and Y. P. Zhao, *Phys. Rev. Lett.*, 2010, **104**.
20. Q. Z. Yuan and Y. P. Zhao, *Nanoscale*, 2015, **7**, 2561-2567.
21. A. Verdaguer, G. M. Sacha, H. Bluhm and M. Salmeron, *Chem. Rev.*, 2006, **106**, 1478-1510.
22. J. Carrasco, A. Hodgson and A. Michaelides, *Nat. Mater.*, 2012, **11**, 667-674.
23. S. Meng, E. G. Wang and S. W. Gao, *Phys. Rev. B*, 2004, **69**, 195404.
24. S. Meng, L. F. Xu, E. G. Wang and S. W. Gao, *Phys. Rev. Lett.*, 2002, **89**, 176104.
25. A. Michaelides, *Appl. Phys. A*, 2006, **85**, 415-425.
26. A. Glebov, A. P. Graham, A. Menzel and J. P. Toennies, *J. Chem. Phys.*, 1997, **106**, 9382-9385.
27. G. A. Kimmel, N. G. Petrik, Z. Dohnalek and B. D. Kay, *Phys. Rev. Lett.*, 2005, **95**, 166102.
28. S. Nie, P. J. Feibelman, N. C. Bartelt and K. Thurmer, *Phys. Rev. Lett.*, 2010, **105**, 026102.
29. J. Chen, G. Schusteritsch, C. J. Pickard, C. G. Salzmann and A. Michaelides, *Phys. Rev. Lett.*, 2016, **116**, 025501.
30. S. Standop, A. Redinger, M. Morgenstern, T. Michely and C. Busse, *Phys. Rev. B*, 2010, **82**, 161412.
31. H. Ogasawara, B. Brena, D. Nordlund, M. Nyberg, A. Pelmenschikov, L. G. M. Pettersson and A. Nilsson, *Phys. Rev. Lett.*, 2002, **89**, 276102.
32. M. L. Liriano, C. Gattinoni, E. A. Lewis, C. J. Murphy, E. C. H. Sykes and A. Michaelides, *J. Am. Chem. Soc.*, 2017, **139**, 6403-6410.
33. K. Andersson, A. Nikitin, L. G. M. Pettersson, A. Nilsson and H. Ogasawara, *Phys. Rev. Lett.*, 2004, **93**, 196101.
34. S. Maier, I. Stass, J. I. Cerda and M. Salmeron, *Phys. Rev. Lett.*, 2014, **112**, 126101.
35. E. Carrasco, A. Aumer, J. F. Gomes, Y. Fujimori and M. Sterrer, *Chem. Comm.*, 2013, **49**, 4355-4357.
36. P. B. Miranda, L. Xu, Y. R. Shen and M. Salmeron, *Phys. Rev. Lett.*, 1998, **81**, 5876-5879.
37. J. J. Yang, S. Meng, L. F. Xu and E. G. Wang, *Phys. Rev. Lett.*, 2004, **92**, 146102.
38. J. Chen, J. Guo, X. Z. Meng, J. B. Peng, J. M. Sheng, L. M. Xu, Y. Jiang, X. Z. Li and E. G. Wang, *Nat. Comm.*, 2014, **5**, 4056.
39. X. Zhang, J. Y. Xu, Y. B. Tu, K. Sun, M. L. Tao, Z. H. Xiong, K. H. Wu, J. Z. Wang, Q. K.

Xue and S. Meng, *Phys. Rev. Lett.*, 2018, **121**, 256001.
40. W. H. Zhao, L. Wang, J. Bai, L. F. Yuan, J. L. Yang and X. C. Zeng, *Acc. Chem. Res.*, 2014, **47**, 2505-2513.
41. W. H. Zhao, J. Bai, L. F. Yuan, J. L. Yang and X. C. Zeng, *Chem. Sci.*, 2014, **5**, 1757-1764.
42. J. Bai, C. A. Angell and X. C. Zeng, *Proc. Natl. Acad. Sci. USA*, 2010, **107**, 5718-5722.
43. R. Zangi and A. E. Mark, *Phys. Rev. Lett.*, 2003, **91**, 025502.
44. A. L. Ferguson, N. Giovambattista, P. J. Rossky, A. Z. Panagiotopoulos and P. G. Debenedetti, *J. Chem. Phys.*, 2012, **137**, 144501.
45. Y. Liu and L. Ojamäe, *Phys. Chem. Chem. Phys.*, 2018, **20**, 8333-8340.
46. Y. Liu, Y. Y. Huang, C. Q. Zhu, H. Li, J. J. Zhao, L. Wang, L. Ojamäe, J. S. Francisco and X. C. Zeng, *Proc. Natl. Acad. Sci. USA*, 2019, **116**, 12684-12691.
47. C. Q. Zhu, Y. R. Gao, W. D. Zhu, J. Jiang, J. Liu, J. J. Wang, J. S. Francisco and X. C. Zeng, *Proc. Natl. Acad. Sci. USA*, 2019, **116**, 16723-16728.
48. X. Y. Zhu, Q. Z. Yuan and Y. P. Zhao, *Nanoscale*, 2014, **6**, 5432-5437.
49. J. L. F. Abascal, E. Sanz, R. G. Fernandez and C. Vega, *J. Chem. Phys.*, 2005, **122**, 234511.
50. C. L. Wang, H. J. Lu, Z. G. Wang, P. Xiu, B. Zhou, G. H. Zuo, R. Z. Wan, J. Z. Hu and H. P. Fang, *Phys. Rev. Lett.*, 2009, **103**, 137801.
51. S. Meng, Z. Y. Zhang and E. Kaxiras, *Phys. Rev. Lett.*, 2006, **97**, 036107.
52. D. Cao, R. Ma, C. Zhu, Y. Tian, J. Peng, J. Guo, J. Chen, X. Z. Li, J. S. Francisco, X. C. Zeng, L. M. Xu, E. G. Wang, Y. Jiang., *Nature*, 2019, accepted.
53. T. Koishi, K. Yasuoka, T. Ebisuzaki, S. Yoo and X. C. Zeng, *J. Chem. Phys.*, 2005, **123**, 204707.
54. D. Van der Spoel, E. Lindahl, B. Hess, G. Groenhof, A. E. Mark and H. J. C. Berendsen, *J. Comput. Chem.*, 2005, **26**, 1701-1718.
55. S. Grimme, J. Antony, S. Ehrlich and H. Krieg, *J. Chem. Phys.*, 2010, **132**, 154104.
56. J. VandeVondele, M. Krack, F. Mohamed, M. Parrinello, T. Chassaing and J. Hutter, *Comput. Phys. Commun.*, 2005, **167**, 103-128.
57. G. Lippert, J. Hutter and M. Parrinello, *Mol. Phys.*, 1997, **92**, 477-487.
58. S. Goedecker, M. Teter and J. Hutter, *Phys. Rev. B*, 1996, **54**, 1703-1710.
59. C. Hartwigsen, S. Goedecker and J. Hutter, *Phys. Rev. B*, 1998, **58**, 3641-3662.
60. J. VandeVondele and J. Hutter, *J. Chem. Phys.*, 2007, **127**, 114105.

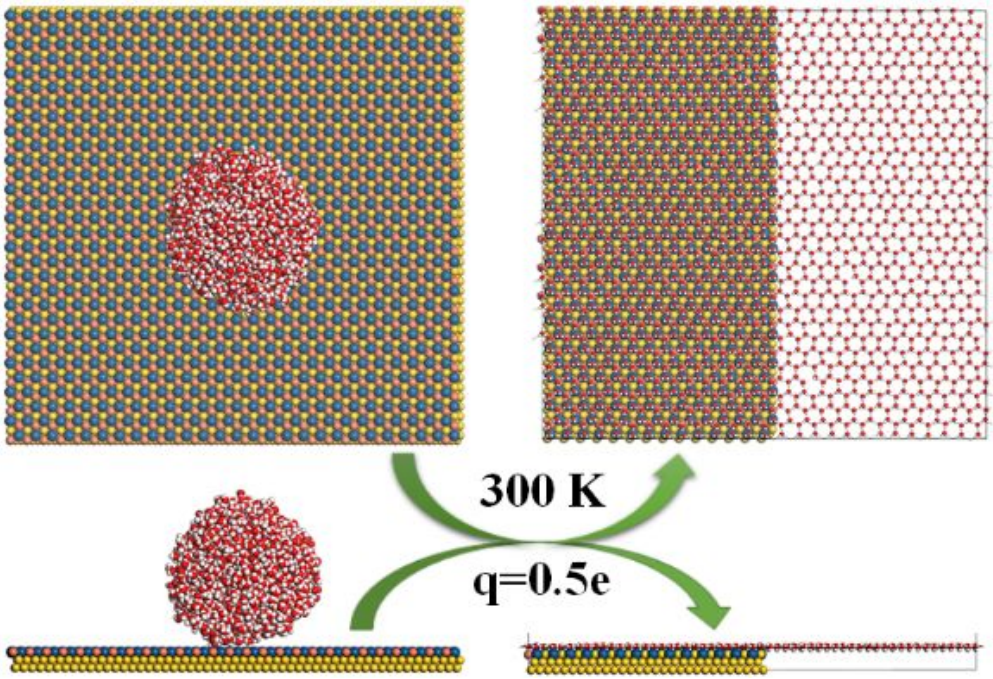
300 K
q=0.5e